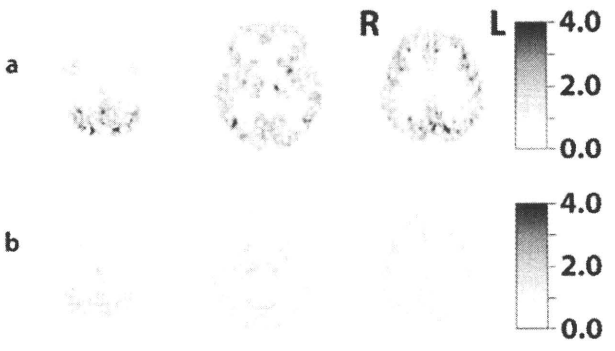

Fig. 2 Positron emission tomography (PET) images for a 65-year-old healthy woman (**a**), and a 71-year-old woman with Alzheimer's disease (**b**). Parametric images for the DVt of [^{11}C]SA4503 were generated using a graphical analysis. [^{11}C]SA4503 PET demonstrates that the sigma$_1$ receptors are widely distributed throughout the entire brain in a normal subject (**a**). In comparison with the normal subject, the number of sigma$_1$ receptors was decreased in the brain of the patient with Alzheimer's disease (**b**)

when the BP in the control subjects (62.6 ± 8.2 years) was compared with that in the young subjects (n = 9, 28 ± 4 years) reported earlier [24], it was found to be slightly decreased with aging without statistical significance (unpublished data) in spite of an age-dependent increase of the [^{11}C]SA4503 binding in rats and monkeys [14, 15]. The reduction of the BP in AD was much more marked compared with the BP in the aged control subjects. Therefore, the reduced sigma$_1$ receptor density in AD could not be derived from the slight difference in age between the control and patient groups. PET with [^{18}F]FDG and statistical image analysis applications such as statistical parametric mapping (SPM) and 3D stereotactic surface projections have shown that in patients with AD, the cerebral glucose metabolism is reduced in the temporal-, parietal-, posterior cingulate-, and prefrontal regions [26, 27]. We also confirmed a similar pattern in the present patients with AD by [^{18}F]FDG PET (data not shown). However, these findings did not correspond with the distribution of neuronal loss on postmortem studies [34]. In a [^{11}C]flumazenil PET study on AD, Ohyama et al. [35] showed that benzodiazepine receptor was less impaired than neuronal function assessed by the cerebral blood flow and glucose metabolism in the association-cortex. The benzodiazepine receptors are one of the gamma-aminobutyric acid type A ($GABA_A$) receptor complex. The present study indicated that sigma$_1$ receptors were affected from the early stages of AD, unlike $GABA_A$ receptors. Some articles showed that the sigma$_1$ receptor agonists increased extracellular acetylcholine levels in the rat frontal cortex and hippocampus [11, 12]. Increased acetylcholine does not directly affect the [^{11}C]SA4503 binding, because acetylcholine does not bind to sigma$_1$ receptors. However, reduction of the number of sigma$_1$ receptors may reflect the cholinergic system and cognitive function of patients with AD. Amyloid imaging by PET currently represents a potentially useful tool for the early diagnosis of pre-onset AD [36]. We have an interest in the relationship between sigma$_1$ receptor in the mild cognitive impairment stage and pre-onset stage of AD. Further studies will be needed using amyloid PET and [^{11}C]SA4503 PET.

The density of sigma$_1$ receptors in the cerebellum was significantly lower in AD than in normals, although K_1 in AD was comparable with that in normals. Although the cerebellum was formerly thought to be unaffected in AD, many studies have revealed cerebellar changes in AD patients [37–43]. A pathological study showed that the density of Purkinje cell was reduced in the cerebellum of AD, especially in the vermis [41]. Using glutamate as the neurotransmitter, the granule cells deliver an excitability signal to the dendrite of Purkinje cells. Chaki et al. [44] suggested that sigma$_1$ binding sites are involved in modulating the release of dopamine by interacting with *N*-methyl-D-aspartic acid (NMDA) receptors on dopaminergic nerve terminals. Release of dopamine is reduced in the putamen with Parkinson's disease, and sigma$_1$ receptors were down-regulated in the putamen with Parkinson's disease [19]. Sigma$_1$ receptors in the cerebellum may be involved in the modulation of glutamate receptor, as well as in the putamen.

Although we could observe a reduced density of sigma$_1$ receptors in the early phase of AD, we cannot say that [^{11}C]SA4503 PET is suitable for the early diagnosis of AD. We are obliged to force the subjects to remain still for over 100 min with their heads fixed in a PET machine and to cannulate their radial artery to sample the arterial blood. Most AD patients are not suitable for the protocol of [^{11}C]SA4503 PET. Prior to the examinations, we had to confirm whether each of the AD subjects in the current study could withstand the protocol of [^{11}C]SA4503 PET. Therefore, we are now investigating a shortened protocol for [^{11}C]SA4503 PET; 40- to 60-min PET scans without arterial blood sampling could possibly provide reliable results in the practical application, which will be described elsewhere.

Acknowledgments This work was supported by a Grant-in-Aid for Scientific Research (B) No. 13557077 from the Japan Society for the Promotion of Science. The authors thank Ms. M. Ando for taking care of the subjects undergoing PET scanning.

References

1. Hashimoto K, Ishiwata K. Sigma receptor ligands: possible application as therapeutic drugs and as radiopharmaceuticals. Curr Pharm Des 2006;12:3857–76.
2. Walker JM, Bowen WD, Walker FO, Matsumoto RR, De Costa B, Rice KC. Sigma receptors: biology and function. Pharmacol Rev 1990;42:355–402.
3. Quirion R, Bowen WD, Itzhak Y, Junien JL, Musacchio JM, Rothman RB, et al. A proposal for the classification of sigma binding sites. Trends Pharmacol Sci 1992;13:85–6.
4. Su TP, London ED, Jaffe JH. Steroid binding at sigma receptors suggests a link between endocrine, nervous, and immune systems. Science (New York) 1988;240:219–21.
5. Su TP. Delineating biochemical and functional properties of sigma receptors: emerging concepts. Critical Rev Neurobiol 1993;7:187–203.
6. Bowen WD. Sigma receptors: recent advances and new clinical potentials. Pharm Acta Helv 2000;7:211–8.
7. Maurice T, Urani A, Phan VL, Romieu P. The interaction between neuroactive steroids and the sigma$_1$ receptor function: behavioral consequences and therapeutic opportunities. Brain Res Rev 2001;37:116–32.
8. Hiramatsu M, Hoshino T, Kameyama T, Nabeshima T. Involvement of kappa-opioid and sigma receptors in short-term memory in mice. Eur J Pharmacol 2002;453:91–8.
9. Maurice T, Hiramatsu M, Kameyama T, Hasegawa T, Nabeshima T. Behavioral evidence for a modulating role of sigma ligands in memory processes: II. Reversion of carbon monoxide-induced amnesia. Brain Res 1994;647:57–64.
10. Senda T, Matsuno K, Okamoto K, Kobayashi T, Nakata K, Mita S. Ameliorating effect of SA4503, a novel sigma$_1$ receptor agonist, on memory impairments induced by cholinergic dysfunction in rats. Eur J Pharmacol 1996;315:1–10.
11. Matsuno K, Matsunaga K, Senda T, Mita S. Increase in extracellular acetylcholine level by sigma ligands in rat frontal cortex. J Pharmacol Exp Ther 1993;265:851–9.
12. Matsuno K, Senda T, Kobayashi T, Mita S. Involvement of sigma$_1$ receptor in (+)-N-allylnormetazocine-stimulated hippocampal cholinergic functions in rats. Brain Res 1995;690:200–6.
13. Kobayashi T, Matsuno K, Nakata K, Mita S. Enhancement of acetylcholine release by SA4503, a novel sigma$_1$ receptor agonist, in the rat brain. J Pharmacol Exp Ther 1996;279:106–13.
14. Ishiwata K, Kobayashi T, Kawamura K, Matsuno K. Age-related changes of the binding of [^{3}H]SA4503 to sigma$_1$ receptors in the rat brain. Ann Nucl Med 2003;17:73–7.
15. Kawamura K, Kimura Y, Tsukada H, Kobayashi T, Nishiyama S, Kakiuchi T, et al. An increase of sigma receptors in the aged monkey brain. Neurobiol Aging 2003;24:745–52.
16. Weissman AD, Casanova MF, Kleinman JE, London ED, De Souza EB. Selective loss of cerebral cortical sigma, but not PCP binding sites in schizophrenia. Biol Psychiatry 1991;29:41–54.
17. Matsuno K, Kobayashi T, Tanaka MK, Mita S. Sigma$_1$ receptor subtype is involved in the relief of behavioral despair in the mouse forced swimming test. Eur J Pharmacol 1996;312:267–71.
18. Lobner D, Lipton P. Sigma-ligands and non-competitive NMDA antagonists inhibit glutamate release during cerebral ischemia. Neurosci Lett 1990;117:169–74.
19. Mishina M, Ishiwata K, Ishii K, Kitamura S, Kimura Y, Kawamura K, et al. Function of sigma receptors in Parkinson's disease. Acta Neurol Scand 2005;112:103–7.
20. Jansen KL, Faull RL, Storey P, Leslie RA. Loss of sigma binding sites in the CA1 area of the anterior hippocampus in Alzheimer's disease correlates with CA1 pyramidal cell loss. Brain Res 1993;623:299–302.
21. Maurice T. Improving Alzheimer's disease-related cognitive deficits with sigma$_1$ receptor agonists. Drug News Perspect 2002;15:617–25.
22. Ishiwata K, Tsukada H, Kawamura K, Kimura Y, Nishiyama S, Kobayashi T, et al. Mapping of CNS sigma$_1$ receptors in the conscious monkey: preliminary PET study with [^{11}C]SA4503. Synapse 2001;40:235–7.
23. Kawamura K, Ishiwata K, Tajima H, Ishii S, Matsuno K, Homma Y, et al. In vivo evaluation of [^{11}C]SA4503 as a PET ligand for mapping CNS sigma$_1$ receptors. Nucl Med Biol 2000;27:255–61.
24. Sakata M, Kimura Y, Naganawa M, Oda K, Ishii K, Chihara K, et al. Mapping of human cerebral sigma$_1$ receptors using positron emission tomography and [^{11}C]SA4503. Neuroimage 2007;35:1–8.
25. McKhann G, Drachman D, Folstein M, Katzman R, Price D, Stadlan EM. Clinical diagnosis of Alzheimer's disease: report of the NINCDS-ADRDA Work Group under the auspices of Department of Health and Human Services Task Force on Alzheimer's Disease. Neurology 1984;34:939–44.
26. Herholz K, Salmon E, Perani D, Baron JC, Holthoff V, Frolich L, et al. Discrimination between Alzheimer dementia and controls by automated analysis of multicenter FDG PET. Neuroimage 2002;17:302–16.
27. Minoshima S, Giordani B, Berent S, Frey KA, Foster NL, Kuhl DE. Metabolic reduction in the posterior cingulate cortex in very early Alzheimer's disease. Ann Neurol 1997;42:85–94.
28. Reisberg B, Borenstein J, Salob SP, Ferris SH, Franssen E, Georgotas A. Behavioral symptoms in Alzheimer's disease: phenomenology and treatment. J Clin Psychiatry 1987;48 Suppl:9–15.
29. Folstein MF, Folstein SE, McHugh PR. "Mini-Mental State". A practical method for grading the cognitive state of patients for the clinician. J Psychiatr Res 1975;12:189–98.
30. Hughes CP, Berg L, Danziger WL, Coben LA, Martin RL. A new clinical scale for the staging of dementia. Br J Psychiatry 1982;140:566–72.
31. Fujiwara T, Watanuki S, Yamamoto S, Miyake M, Seo S, Itoh M, et al. Performance evaluation of a large axial field-of-view PET scanner: SET-2400 W. Ann Nucl Med 1997;11:307–13.
32. Mishina M, Senda M, Kimura Y, Toyama H, Ishiwata K, Ohyama M, et al. Intrasubject correlation between static scan and distribution volume images for [^{11}C]flumazenil PET. Ann Nucl Med 2000;14:193–8.
33. Logan J. A review of graphical methods for tracer studies and strategies to reduce bias. Nucl Med Biol 2003;30:833–44.
34. Mielke R, Schroder R, Fink GR, Kessler J, Herholz K, Heiss WD. Regional cerebral glucose metabolism and postmortem pathology in Alzheimer's disease. Acta Neuropathol (Berl) 1996;91:174–9.
35. Ohyama M, Senda M, Ishiwata K, Kitamura S, Mishina M, Ishii K, et al. Preserved benzodiazepine receptors in Alzheimer's disease measured with C-11 flumazenil PET and I-123 iomazenil SPECT in comparison with CBF. Ann Nucl Med 1999;13:309–15.
36. Nordberg A. PET imaging of amyloid in Alzheimer's disease. Lancet Neurol 2004;3:519–27.
37. Braak H, Braak E, Bohl J, Lang W. Alzheimer's disease: amyloid plaques in the cerebellum. J Neurol sci 1989;93:277–87.

38. Ishii K, Sasaki M, Kitagaki H, Yamaji S, Sakamoto S, Matsuda K, et al. Reduction of cerebellar glucose metabolism in advanced Alzheimer's disease. J Nucl Med 1997;38:925–8.
39. Larner AJ. The cerebellum in Alzheimer's disease. Dement Geriatr Cogn Disord 1997;8:203–9.
40. Wegiel J, Wisniewski HM, Dziewiatkowski J, Badmajew E, Tarnawski M, Reisberg B, et al. Cerebellar atrophy in Alzheimer's disease-clinicopathological correlations. Brain Res 1999;818:41–50.
41. Sjöbeck M, Englund E. Alzheimer's disease and the cerebellum: a morphologic study on neuronal and glial changes. Dement Geriatr Cogn Disord 2001;12:211–8.
42. Verdile G, Gnjec A, Miklossy J, Fonte J, Veurink G, Bates K, et al. Protein markers for Alzheimer disease in the frontal cortex and cerebellum. Neurology 2004;63:1385–92.
43. Sultana R, Boyd-Kimball D, Poon HF, Cai J, Pierce WM, Klein JB, et al. Redox proteomics identification of oxidized proteins in Alzheimer's disease hippocampus and cerebellum: an approach to understand pathological and biochemical alterations in AD. Neurobiol Aging 2006;27:1564–76.
44. Chaki S, Okuyama S, Ogawa S, Tomisawa K. Regulation of NMDA-induced [^{3}H]dopamine release from rat hippocampal slices through sigma-1 binding sites. Neurochem Int 1998;33: 29–34.

ELSEVIER

NeuroImage

www.elsevier.com/locate/ynimg
NeuroImage 40 (2008) 26–34

Robust estimation of the arterial input function for Logan plots using an intersectional searching algorithm and clustering in positron emission tomography for neuroreceptor imaging

Mika Naganawa,[a,b] Yuichi Kimura,[a,*] Junichi Yano,[c] Masahiro Mishina,[d] Masao Yanagisawa,[c] Kenji Ishii,[e] Keiichi Oda,[e] and Kiichi Ishiwata[e]

[a]*Molecular Imaging Center, National Institute of Radiological Sciences, 4-9-1, Anagawa, Inage, Chiba-shi, Chiba, 263-8555, Japan*
[b]*Yale PET Center, School of Medicine, Yale University, New Haven, CT, USA*
[c]*Graduate School of Science and Engineering, Waseda University, Tokyo, Japan*
[d]*Neurological Institute, Nippon Medical School Chiba-Hokusoh Hospital, Chiba, Japan*
[e]*Positron Medical Center, Tokyo Metropolitan Institute of Gerontology, Tokyo, Japan*

Received 9 June 2007; revised 22 October 2007; accepted 17 November 2007
Available online 4 December 2007

The Logan plot is a powerful algorithm used to generate binding-potential images from dynamic positron emission tomography (PET) images in neuroreceptor studies. However, it requires arterial blood sampling and metabolite correction to provide an input function, and clinically it is preferable that this need for arterial blood sampling be obviated. Estimation of the input function with metabolite correction using an intersectional searching algorithm (ISA) has been proposed. The ISA seeks the input function from the intersection between the planes spanned by measured radioactivity curves in tissue and their cumulative integrals in data space. However, the ISA is sensitive to noise included in measured curves, and it often fails to estimate the input function. In this paper, we propose a robust estimation of the cumulative integral of the plasma time–activity curve (pTAC) using ISA (robust EPISA) to overcome noise issues. The EPISA reduces noise in the measured PET data using averaging and clustering that gathers radioactivity curves with similar kinetic parameters. We confirmed that a little noise made the estimation of the input function extremely difficult in the simulation. The robust EPISA was validated by application to eight real dynamic [^{11}C]TMSX PET data sets used to visualize adenosine A_{2A} receptors and four real dynamic [^{11}C]PIB PET data sets used to visualize amyloid-beta plaque. Peripherally, the latter showed faster metabolism than the former. The clustering operation improved the signal-to-noise ratio for the PET data sufficiently to estimate the input function, and the calculated neuroreceptor images had a quality equivalent to that using measured pTACs after metabolite correction. Our proposed method noninvasively yields an alternative input function for Logan plots, allowing the Logan plot to be more useful in neuroreceptor studies.

Keywords: Positron emission tomography; Clustering; Intersectional searching algorithm; Arterial blood sampling; Logan plot

Introduction

The Logan plot (Logan et al., 1990) is a graphical approach that estimates volume of distribution (V_T) from the slope of a plot. V_T refers to the sum of the volume of distributions in the free, nonspecific binding, and specific binding compartments (Koeppe et al., 1991; Innis et al., 2007). Because this algorithm achieves more robust and faster estimation compared with nonlinear least squares methods (Carson, 2002), it is widely used for generating parametric images of V_T in neuroreceptor mapping. The Logan plot requires two measurable data sets: one is obtained by dynamic PET scanning, and the other is obtained by serial arterial blood sampling. If the serial arterial blood sampling can be omitted, the Logan plot becomes a more useful and easy-to-use approach. There are several approaches to avoiding invasive arterial blood sampling. Reference-region-based Logan plot (Logan et al., 1996) cancels out the term of the integral of the plasma time–activity curve (pTAC) using a tissue time–activity curve (tTAC) in reference regions where the target receptor is negligible. Although the term relating to the pTAC is expelled, the estimation equation still includes an efflux parameter, k_2 [1/min]. It is sometimes difficult to know the value of k_2 about reference regions in advance. If an equilibrium state is achieved between tTAC and pTAC, a priori knowledge of k_2 is not necessary, but such a

* Corresponding author.
E-mail address: ukimura@ieee.org (Y. Kimura).
Available online on ScienceDirect (www.sciencedirect.com).

1053-8119/$ - see front matter © 2007 Elsevier Inc. All rights reserved.
doi:10.1016/j.neuroimage.2007.11.035

situation is not always realized. Another approach, which we have previously proposed, is based on a statistical model: independent component analysis (Naganawa et al., 2005a,b) and variational Bayes (Naganawa et al., 2007a). These methods assume a factor analysis model in which each voxel includes the radioactivities from tissue and blood, and estimates the time–activity curve (TAC) of whole blood radioactivity. The estimated blood curve was successfully used in Logan plots as an alternative to the measured pTAC. Note that the plasma-to-whole blood ratio should be constant in the time for which the Logan plot was applied (Naganawa et al., 2005b), and the estimated blood curve includes the radioactivity in metabolites.

In applying the Logan plot, an input blood function appears in a form of the cumulative integral of the pTAC (intpTAC). It is desirable for the intpTAC to be corrected metabolically. Wang et al. proposed an intersectional searching algorithm (ISA) to estimate the intpTAC directly (Wang et al., 2005). The metabolite-corrected intpTAC will be theoretically obtained using their algorithm. However, one aspect to be considered is noise in the measured tTACs. Because of its mathematical nature, the ISA is very sensitive to noise, and it is thus important to reduce the noise effectively in estimating intpTAC. We have developed methods to reduce the measurement noise using clustering based on each TAC's kinetics (Kimura et al., 1999, 2005a,b). It is expected that our clustering method will improve estimation using ISA. In this paper, we propose a method for robust extraction of the intpTAC using ISA and clustering (robust EPISA). We clarify the sensitivity of the ISA to the measurement noise using simulations, and we investigate the applicability of the robust EPISA by applying it to dynamic PET data using [7-methyl-^{11}C]-(*E*)-8-(3,4,5-trimethoxystyryl)-1,3,7-trimethylxanthine ([^{11}C]TMSX), which visualizes adenosine A_{2A} receptors (Ishiwata et al., 2000, 2005; Mishina et al., 2007), and [*N*-methyl-^{11}C]2-(4′-methylaminophenyl)-6-hydroxy-benzothiazole] ([^{11}C]PIB), which visualizes amyloid-beta plaque (Mathis et al., 2003; Klunk et al., 2004).

Theory

ISA

ISA (Wang et al., 2005) estimates the intpTAC using at least two tTACs with mutually different shapes and the corresponding cumulative integral of the tTACs (inttTAC) based on the equations for the Logan plot. This section provides an overview of the ISA and discusses its drawbacks. The equation for the Logan plot is described as

$$\frac{\int_0^T c^{(i)}(t)\mathrm{d}t}{c^{(i)}(T)} = d^{(i)}\frac{\int_0^T c_p(t)\mathrm{d}t}{c^{(i)}(T)} + b^{(i)}, \tag{1}$$

where $c^{(i)}(t)$ is a tTAC at the ith voxel or region and $c_p(t)$ is a pTAC. $\int_0^T c^{(i)}(t)\mathrm{d}t$ and $\int_0^T c_p(t)\mathrm{d}t$ are inttTAC at the ith voxel and intpTAC, respectively. For time $T \geq t^*$, the second term $b^{(i)}$ (<0) is a constant, and $d^{(i)}$ corresponds to a V_T. Eq. (1) is arranged for $\int_0^T c_p(t)\mathrm{d}t$ as

$$\begin{aligned}\int_0^T c_p(t)\mathrm{d}t &= \frac{-b^{(i)}}{d^{(i)}}c^{(i)}(T) + \frac{1}{d^{(i)}}\int_0^T c^{(i)}(t)\mathrm{d}t \\ &= a_1^{(i)}c^{(i)}(T) + a_2^{(i)}\int_0^T c^{(i)}(t)\mathrm{d}t.\end{aligned} \tag{2}$$

Because the values of $d^{(i)}$ and $b^{(i)}$ are constant, constant coefficients $-b^{(i)}/d^{(i)}$ and $1/d^{(i)}$ are denoted as $a_1^{(i)}$ and $a_2^{(i)}$, respectively. Assuming that a tTAC is measured at times $T=t_1, t_2, \ldots, t_m$, Eq. (2) can be written in terms of vectors as

$$\boldsymbol{c}_{\mathrm{pint}} = a_1^{(i)}\boldsymbol{c}^{(i)} + a_2^{(i)}\boldsymbol{c}_{\mathrm{int}}^{(i)}, \tag{3}$$

where $\boldsymbol{c}_{\mathrm{pint}}$, $\boldsymbol{c}^{(i)}$, and $\boldsymbol{c}_{\mathrm{int}}^{(i)}$ are column vectors of m elements corresponding to $\int_0^T c_p(t)\mathrm{d}t$, $c^{(i)}(T)$, and $\int_0^T c^{(i)}(t)\mathrm{d}t$, respectively. Because $\boldsymbol{c}_{\mathrm{pint}}$ is a common vector between the ith and jth voxels or regions ($i \neq j$), the following equation is obtained.

$$a_1^{(i)}\boldsymbol{c}^{(i)} + a_2^{(i)}\boldsymbol{c}_{\mathrm{int}}^{(i)} = a_1^{(j)}\boldsymbol{c}^{(j)} + a_2^{(j)}\boldsymbol{c}_{\mathrm{int}}^{(j)} \tag{4}$$

Eq. (4) can be rewritten as

$$(\boldsymbol{c}^{(i)}\boldsymbol{c}_{\mathrm{int}}^{(i)}\boldsymbol{c}^{(j)}\boldsymbol{c}_{\mathrm{int}}^{(j)})\begin{pmatrix} a_1^{(i)} \\ a_2^{(i)} \\ -a_1^{(j)} \\ -a_2^{(j)} \end{pmatrix} = \boldsymbol{C}\boldsymbol{a} = 0, \tag{5}$$

where $\boldsymbol{C} \in \mathcal{R}^{m\times 4}$ is a matrix ($m>4$) and $\boldsymbol{a} \in \mathcal{R}^{4\times 1}$ is a column vector. Because the rank of the matrix $\boldsymbol{C}$ is at most three, the vector $\boldsymbol{a}$ can be estimated as a right singular vector corresponding to the smallest right singular value of $\boldsymbol{C}$. Because any vector whose direction is equal to the right singular vector $\boldsymbol{a}$ satisfies Eq. (5), the length of $\boldsymbol{a}$ cannot be determined. Accordingly, the absolute value of the intpTAC cannot be determined. ISA infers only the shape of the intpTAC during the period in which the Logan plot can be applied. Although the absolute value of the V_T at each voxel cannot be determined using the Logan plot with ISA-estimated intpTAC, the ratio between them can be estimated. Note that the estimation of the intpTAC is limited to the range of time used for the Logan plot, because ISA is defined only on the frames where the Logan plot is applicable. Thus, ISA is useless in estimating the intpTAC at early times, and the estimated intpTAC cannot be used as an input function for the nonlinear least squares method.

Let us give a geometrical interpretation of ISA algorithm to allow intuitive understanding of the effect of noise. Eq. (3) means that the intpTAC vector $\boldsymbol{c}_{\mathrm{pint}}$ is on the plane that is spanned by the tTAC vector $\boldsymbol{c}^{(i)}$ and the inttTAC vector $\boldsymbol{c}^{(i)}$. Eq. (4) shows that $\boldsymbol{c}_{\mathrm{pint}}$ is an intersectional vector of two planes by the i and jth voxel. Fig. 1 shows the geometric relationship between intpTAC, the tTACs and the inttTACs. In reality, there is a large amount of noise in the measured PET data. Therefore, the plane spanned by the tTAC vector and the inttTAC vector is deviated from the true plane. Accordingly, the measurement noise produces estimation error in the direction of the intersectional vector $\boldsymbol{c}_{\mathrm{pint}}$.

Robust EPISA

The proposed method, robust EPISA, improves the signal-to-noise ratio of the measured PET data using averaging and clustering. The voxels that locate close to each other tend to have similar kinetics. In addition, there exist tTACs that have similar kinetics but locate at separate positions. In robust EPISA, first, a spatial averaging filter is applied. Clustering is subsequently performed to gather tTACs based on their kinetics, and tTACs classified into the same cluster are averaged. Finally,

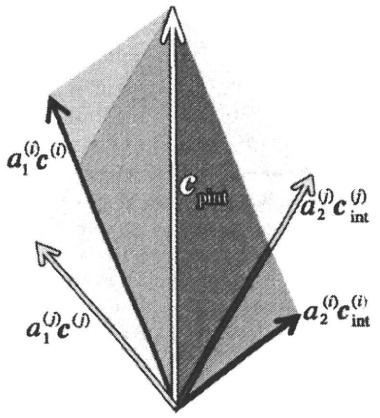

Fig. 1. Schematic illustration of a relationship between intpTAC, the tTACs, and the inttTACs. The intpTAC is estimated as an intersection vector of two planes.

the intersection-searching algorithm is applied to noise-reduced data.

To reduce noise, clustering was performed using a quantity proposed in (Kimura et al., 1999, 2002). The quantity, R, is defined as

$$R \equiv \frac{\int_0^T c^{(i)}(t)\mathrm{d}t}{\int_0^T tc^{(i)}(t)\mathrm{d}t} \tag{6}$$

where T is the time of the final frame. The amplitude of R is determined by only the shape of the tTAC emphasized by t. The quantity R is invariant when the tTAC becomes the product of a constant α times the tTAC $c^{(i)}(t)$, because α is canceled out between the numerator and the denominator in Eq. (6). Therefore, the quantity R evaluates the tTAC's shape. For example, the quantity R becomes a function of a kinetic efflux parameter k_2 when a kinetic of the administered radioligand is described by a one-tissue two-compartment model (Kimura et al., 1999).

The actual procedures in robust EPISA are shown below.

1. The region outside the brain was excluded and voxel-based PET data were spatially averaged.
2. The quantity, R, was calculated about each voxel, and voxels with similar R were categorized into one cluster. The same number of voxels were assigned to each cluster.
3. The tTACs categorized into the same cluster were averaged. Note that each tTAC was normalized by each time integral.
4. The intpTACs were estimated from all possible pairs of the averaged tTACs.
5. The candidate intpTACs were obtained from all estimated intpTACs by excluding failed curves, and the final result was the averaged candidate intpTACs.

A suitable size of clusters for Step 2 was investigated. An intpTAC should be a monotonically increasing function with positive values. The failed curves in Step 5 mean the intpTACs with negative values or the intpTACs that do not monotonically increase. In Step 5, a scale of the intpTAC should be normalized before averaging because it cannot be determined using ISA.

Materials and methods

Simulations

Simulations were carried out to investigate the behavior of the ISA in the presence of noise to make sure of the necessity of noise reduction in applying ISA. Perfect tTACs were generated using a metabolite-corrected pTAC obtained from a human [^{11}C]TMSX study with serial arterial blood sampling. Kinetic parameter values of [^{11}C]TMSX in the putamen and the frontal lobe (Naganawa et al., 2007b) were chosen for the generation of noise-free tTACs (K_1=0.32 (mL plasma)·min^{-1} (mL tissue)$^{-1}$, k_2=0.43 min^{-1}, k_3=0.44 min^{-1}, k_4=0.36 min^{-1} and K_1=0.29 (mL plasma)·min^{-1} (mL tissue)$^{-1}$, k_2=0.39 min^{-1}, k_3=0.13 min^{-1}, k_4=0.29 min^{-1}, respectively). Noisy data were subsequently obtained by adding Gaussian noise to the noise-free data. Added noise was expressed as $\mathcal{N}\left(0, \beta\frac{c(t)}{\Delta t}\right)$, where Δt is the frame width and β is a proportional constant that represents the noise level. The simulations were conducted for a protocol of 27 frames over a period of 1 h (10 s × 6, 30 s × 3, 60 s × 5, 150 s × 5, and 5 min × 8). The noise level β was set to be 0 and 16. The noise level was scaled so that the value of 16 corresponded to the averaged tTAC over 100 voxels. In the simulation, 20 realizations of noisy tTACs were generated, and 10 pairs of tTACs were randomly selected from the tTACs, and ISA was applied to them because an intpTAC is estimated using two tTACs in EPISA. ISA was also applied to noise-free tTACs. Because it is possible to apply Logan plots to [^{11}C]TMSX 10 min after administration (Naganawa et al., 2007b), ISA was performed using the simulated data between 27.5 and 57.5 min after administration. The estimated intpTACs were compared with the true intpTAC.

[^{11}C]TMSX PET studies

The presented method (robust EPISA) was applied to eight human [^{11}C]TMSX PET data sets in order to investigate the effects of averaging and clustering. The Ethics Committee of Tokyo Metropolitan Institute of Gerontology approved the study protocol. [^{11}C]TMSX PET data were acquired from seven healthy volunteers and one patient with Parkinson's disease. Written informed consent was obtained from all subjects before the study. After a transmission scan, 590 ± 103 MBq of [^{11}C]TMSX with a specific activity of 40 ± 21 GBq/μmol was administered intravenously, and a 1 h dynamic PET scan was performed in two-dimensional mode using a SET-2400W (Shimadzu Co., Kyoto, Japan). The acquisition consisted of 27 frames of data (10 s × 6, 30 s × 3, 60 s × 5, 150 s × 5, and 5 min × 8). The dynamic PET data were reconstructed using a filtered back-projection algorithm with a second-order low-pass filter with a cutoff frequency of 1.25 cycles/cm. Twenty-five slices were scanned–each slice with 96 × 96 voxels–and the resulting voxel size was 2 × 2 × 6.25 mm. Serial arterial blood sampling and metabolite analysis were performed during the scan. Arterial blood samples were taken from the brachial artery at 10, 20, 30, 40, 50, 60, 70, 80, 90, 100, 110, 120, 135 and 150 s and 3, 5, 7, 10, 15, 20, 30, 40, 50 and 60 min. The radioactivity in the plasma was measured using a well-type gamma counter (BSS-1, Shimadzu Co., Kyoto, Japan) against which the PET camera was cross-calibrated. The unmetabolized fraction was measured by high-performance liquid chromatography (Ishiwata et al., 2003). The unmetabolized fraction in the plasma samples was fitted to the function proposed in Watabe et al. (2000).

Fifteen slices that cover the whole brain were used for estimation by robust EPISA. The regions outside the brain were specified as the voxels below the 70th percentile of the summed PET images and were excluded from the target of the robust EPISA. Approximately 63,000 voxels were used for the estimation. The 5-by-5 average filter was applied to the measured PET images to improve the signal-to-noise ratio by spatial averaging. The number of clusters was set to 50, and approximately 1250 voxels were included in one cluster. Thus, sufficiently noise-reduced tTACs were obtained. PET images taken between 27.5 and 57.5 min after administration were used in the ISA. The estimated intpTAC was divided by its value at the last frame for normalization. Logan plot was applied to obtain the V_T image using the metabolite-corrected intpTAC and the estimated intpTAC. The centrum semiovale was manually defined as a reference region, and the binding potential, BP_{ND}, image was given by $\frac{V_T}{V_{ND}} - 1$ where V_{ND} is the averaged V_T over the centrum semiovale.

[^{11}C]PIB PET studies

The peripheral metabolism of [^{11}C]TMSX is slow; more than 95% of administered [^{11}C]TMSX remains as the intact form at 60 min post injection (Naganawa et al., 2007b). Therefore, the measured pTACs with and without metabolite correction have similar shape in [^{11}C]TMSX data. In order to investigate the influence of metabolites included in plasma and the number of clusters, the robust EPISA was also applied to four human [^{11}C]PIB PET data sets with faster metabolism. Parent fraction of [^{11}C]PIB was 48±13% at 20 min and 30±8% at 60 min post injection. The Ethics Committee of Tokyo Metropolitan Institute of Gerontology approved the study protocol. [^{11}C]PIB PET data were acquired from two healthy volunteers and two patients with Alzheimer disease who met the criteria of probable AD by NINDS-ADRDA and Dementia of Alzheimer's Type with DSM-IV. Written informed consent was obtained from all subjects before the study. After a transmission scan, 455±55 MBq of [^{11}C]PIB with a specific activity of 88±32 GBq/μmol was administered intravenously, and a 1 h dynamic PET scan was performed in three-dimensional mode using the same scanner as [^{11}C]TMSX scan. The acquisition consisted of 23 frames of data (10 s×6, 20 s×3, 60 s×2, 2 min×1, 4 min×1, and 5 min×10). Image reconstruction, serial arterial blood sampling and metabolite analysis were conducted in the same way as [^{11}C]TMSX scan, and 50 slices were scanned.

Slices that cover the whole brain were used for estimation by robust EPISA. The regions outside the brain were specified as the voxels below the 80th percentile of the summed PET images and were excluded from the target of the robust EPISA. Approximately 126,000 voxels were used for the estimation. The 9-by-9 average filter was applied to the measured PET images. The number of clusters was set to 10 (12,600 voxels/cluster), 20 (6300 voxels/cluster), 40 (3150 voxels/cluster) and 80 (1575 voxels/cluster). ISA was applied to PET images taken between 37.5 and 57.5 min after administration (Price et al., 2005; Lopresti et al., 2005). The estimated intpTAC was divided by its value at the last frame for normalization. Logan plot was applied to obtain the V_T image using the metabolite-corrected intpTAC and the estimated intpTAC. The cerebellum was manually defined as a reference region (Price et al., 2005), and the distribution volume ratio (DVR) image was calculated.

Results

Simulation

The noise sensitivity of the ISA was confirmed using the simulated [^{11}C]TMSX data. The noise-free tTACs and examples of noise-added tTACs used for the simulation are presented in Fig. 2. Fig. 3 shows the estimated intpTACs and the true intpTAC. The scale was adjusted so that the value at the last frame corresponds to that of the true intpTAC. There was no difference between the ISA-estimated intpTAC and the true intpTAC with noise-free data. However, the estimated intpTACs were apparently deviated from the true intpTAC with a noise level of 16.

[^{11}C]TMSX PET studies

Clustering results are shown in Figs. 4 and 5. In Fig. 5, the voxels that have larger clustering criterion R are represented in a brighter color. While the neighboring voxels tend to belong to the same cluster and brain structure can be observed in Fig. 5, some remote voxels were also categorized into the same cluster. The intpTAC was estimated from the clustered and averaged tTACs as shown in Fig. 4. The noise level in the cluster-averaged tTACs was well suppressed. The estimated intpTACs using the proposed robust EPISA is demonstrated with standard deviation in Fig. 6(A). Note that standard deviation was not calculated from all estimated intpTACs but the candidate intpTACs as described in Step 5 in the Robust EPISA section. The estimated intpTACs were similar to the measured intpTACs with metabolite correction. The scale of the robust EPISA estimated intpTAC cannot be determined. In order to compare the estimated intpTACs with the measured intpTACs, the estimated intpTACs were scaled using the value at the last frame. The measured intpTACs without metabolite correction were also scaled using the value at the last frame. It took 5 to 7 s to estimate the intpTAC from one subject's data. The Logan plot was applied to the measured PET data to generate the V_T parametric images, and Fig. 7 shows BP_{ND} images calculated using the estimated V_T

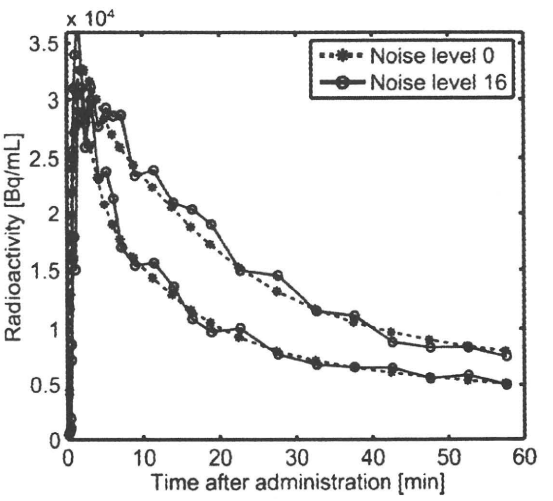

Fig. 2. Example of noise-free tTACs (dashed lines) and noisy tTACs (solid lines) for the simulation investigating the influence of noise in tTACs. The noise level of the noisy tTACs was set to 16. Two kinds of tTACs were used for estimation using ISA.

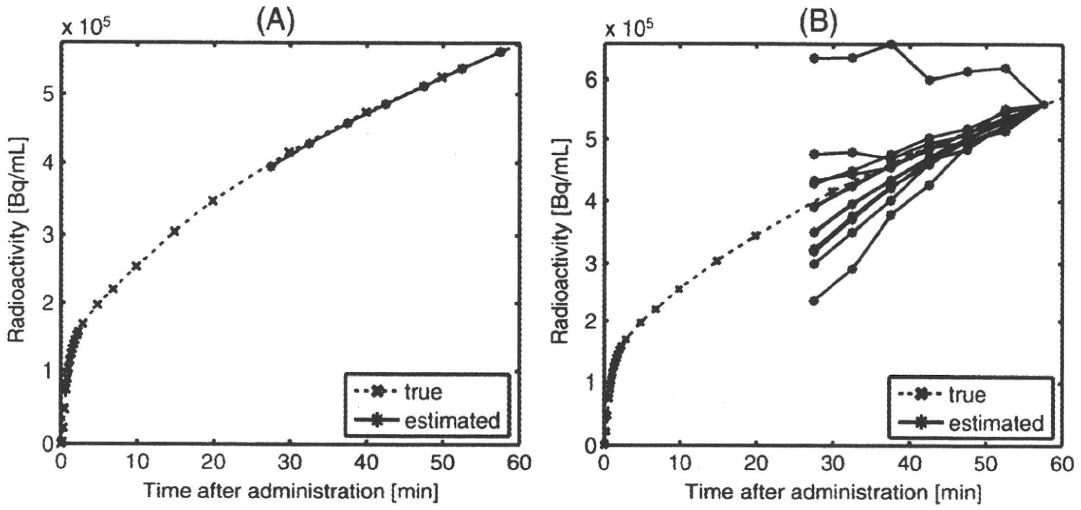

Fig. 3. Estimated intpTACs from the noise-free data (A) and the noisy data (B). The period used for the ISA was 27.5 min to 57.5 min after administration. The true intpTAC was obtained by cumulatively integrating the true pTAC. The estimated intpTACs are shown as solid lines, and the true intpTACs are shown as dashed lines. The scale of the estimated intpTAC was adjusted using the value at the last frame.

parametric images and the specified reference region. The BP_{ND} images with the estimated and measured intpTACs matched well in all eight subjects. In the linear regression between the measured and estimated BP_{ND} images, the slopes and y-intercepts were 1.00 ± 0.011 and 0.035 ± 0.016, respectively. The coefficient of determination (r^2) was 1.00 ± 0.0016.

[^{11}C]PIB PET studies

Fig. 6(B) shows the estimated intpTAC and the standard deviation calculated from candidate intpTACs. The estimated intpTACs were similar to the measured intpTACs with metabolite correction. For comparison, the scale of the estimated intpTACs and the measured intpTACs without metabolite correction was adjusted using the value at the last frame of the measured intpTACs with metabolite correction. The calculation time was comparable to [^{11}C]TMSX study. The relationship between the number of clusters and estimation results were demonstrated in Fig. 8. Standard deviation increased as the size of the clusters became smaller. However, the final estimated intpTAC was little influenced by the choice of the number of clusters. In each case with different number of clusters, the candidate intpTACs from which the final result was obtained were approximately 22% curves out of all estimated intpTACs. When the number of the clusters set to be less than 5, the proposed method did not work. The Logan plot was applied to the measured PET data to generate the V_T parametric images, and Fig. 9 shows the DVR images of Alzheimer disease patient that were calculated using the estimated V_T parametric images in case of 20 clusters. The DVR images with the estimated and measured intpTACs matched well in all four subjects. In the linear regression between the measured and estimated DVR images, the slopes and y-intercepts were 0.97 ± 0.038 and 0.060 ± 0.057, respectively. The coefficient of determination (r^2) was 0.97 ± 0.026.

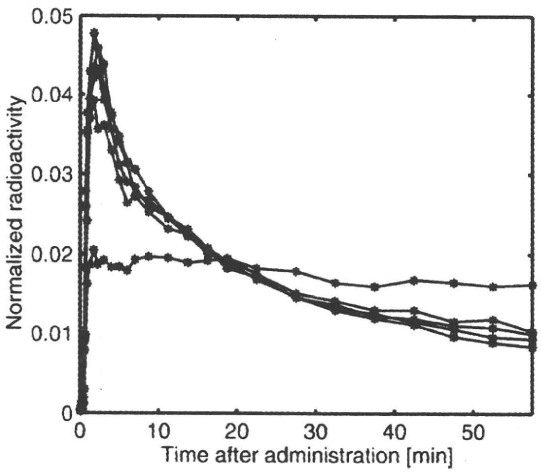

Fig. 4. Representative tTACs after clustering in [^{11}C]TMSX data. The tTACs of the measured PET data were categorized into 50 clusters and subsequently averaged in each cluster. Each tTAC was normalized by dividing by its integral.

Discussion

The proposed method, robust EPISA, settles the mathematical drawback in ISA, in that performance is influenced by the noise in the measured tTACs. The measurement noise included in PET data was reduced by clustering based on tTAC's kinetics, and an input function for Logan plots was estimated robustly based on ISA (Wang et al., 2005). Robust EPISA estimates a shape of a cumulative integral curve of pTAC appearing in the operational equation of the Logan plot, and enables binding-potential imaging to be generated with no arterial blood sampling or metabolite correction. Omission of arterial blood sampling reduces the invasiveness of PET measurement and contributes to the shortened total time needed for preparation of serial arterial blood sampling. Before discussing the robustness of the proposed method, we should consider the advantages and disadvantages of ISA.

ISA has two advantages: no requirement for metabolite correction of pTAC and wide applicability to PET data with various radioligands, because of the broad application of the Logan

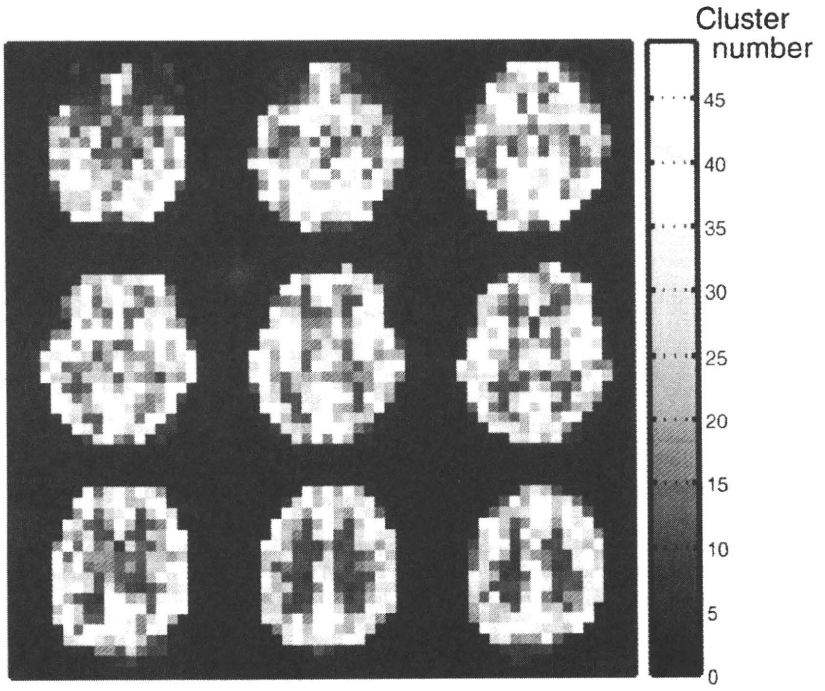

Fig. 5. Example of a clustered image in [^{11}C]TMSX data. The voxel value corresponds to the cluster number. As the cluster number becomes larger, the corresponding criterion R also becomes larger.

plot. Many methods have been proposed to preclude arterial blood sampling. One of these methods is based on a factor model to estimate the shape of a whole blood curve (Barber, 1980; Paola et al., 1982; Wu et al., 1995; Lee et al., 2001; Naganawa et al., 2005a,b), where the radioactivity in the measured PET data is assumed to be the sum of the radioactivities in the blood and tissue. In this method, metabolite correction is unattainable. On the other hand, ISA can theoretically give a metabolite-corrected pTAC. ISA is derived from the operational equation for the Logan plot, and the equations of the Logan plot are based on a compartment model. Thus, the estimated intpTAC does not include the radioactivity in metabolites. There is a great difference between the measured intpTAC with and without metabolite correction in [^{11}C]PIB data. The estimated intpTAC matched well with the measured intpTAC with metabolite correction as shown in Fig. 6. From our results, the estimated BP_{ND} of [^{11}C]TMSX (Fig. 7) or DVR of [^{11}C]PIB (Fig. 9) using the proposed method coincide well with those using a measured pTAC with metabolite correction. It is expected that ISA

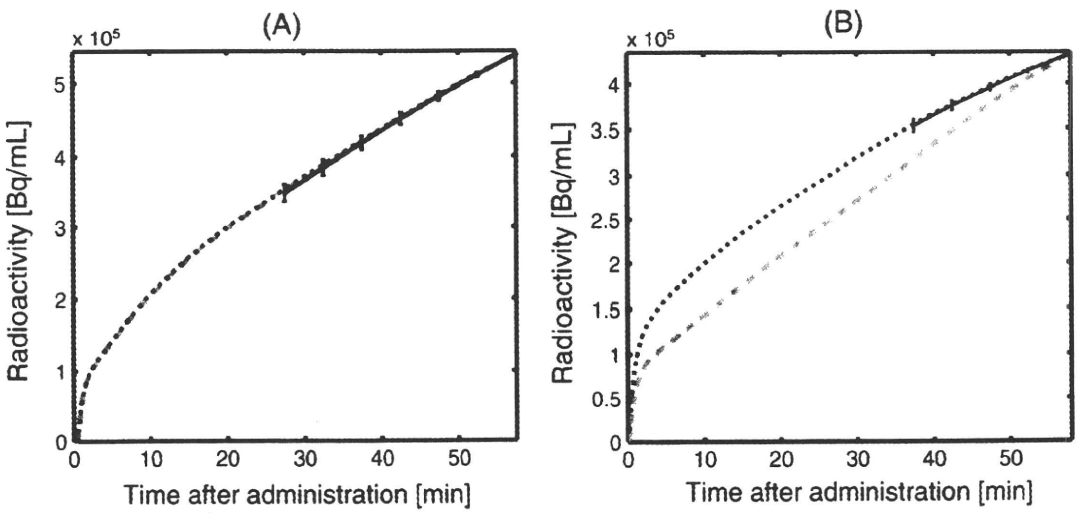

Fig. 6. Example of a robust EPISA-estimated intpTAC (black solid line) in (A) [^{11}C]TMSX and (B) [^{11}C]PIB. In [^{11}C] PIB, 40 clusters were used for clustering. Measured intpTACs with and without metabolite correction were plotted in black dotted line and gray break line, respectively. Standard deviation was calculated from the candidate intpTACs.

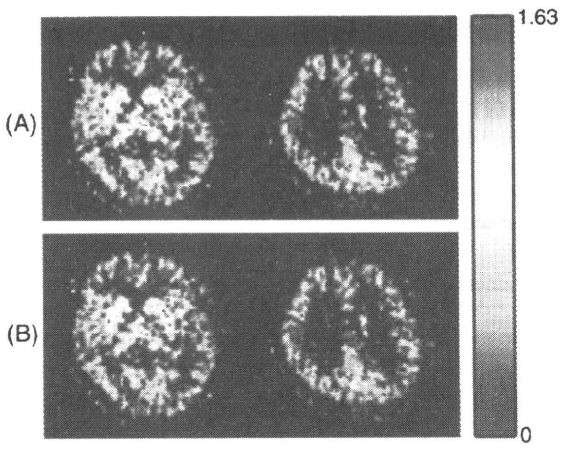

Fig. 7. Example of the parametric images of the BP_{ND} in [^{11}C]TMSX PET data using the robust EPISA-estimated intpTAC (A) and the measured intpTAC with metabolite correction (B). These images were calculated from the V_T images and a reference region.

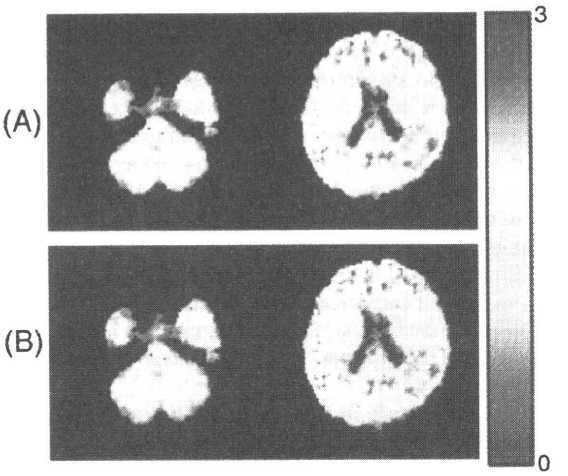

Fig. 9. Example of the parametric images of [^{11}C]PIB DVR in brain with Alzheimer disease. These images were calculated from the V_T images and a reference region using the robust EPISA-estimated intpTAC (A) and the measured intpTAC with metabolite correction (B).

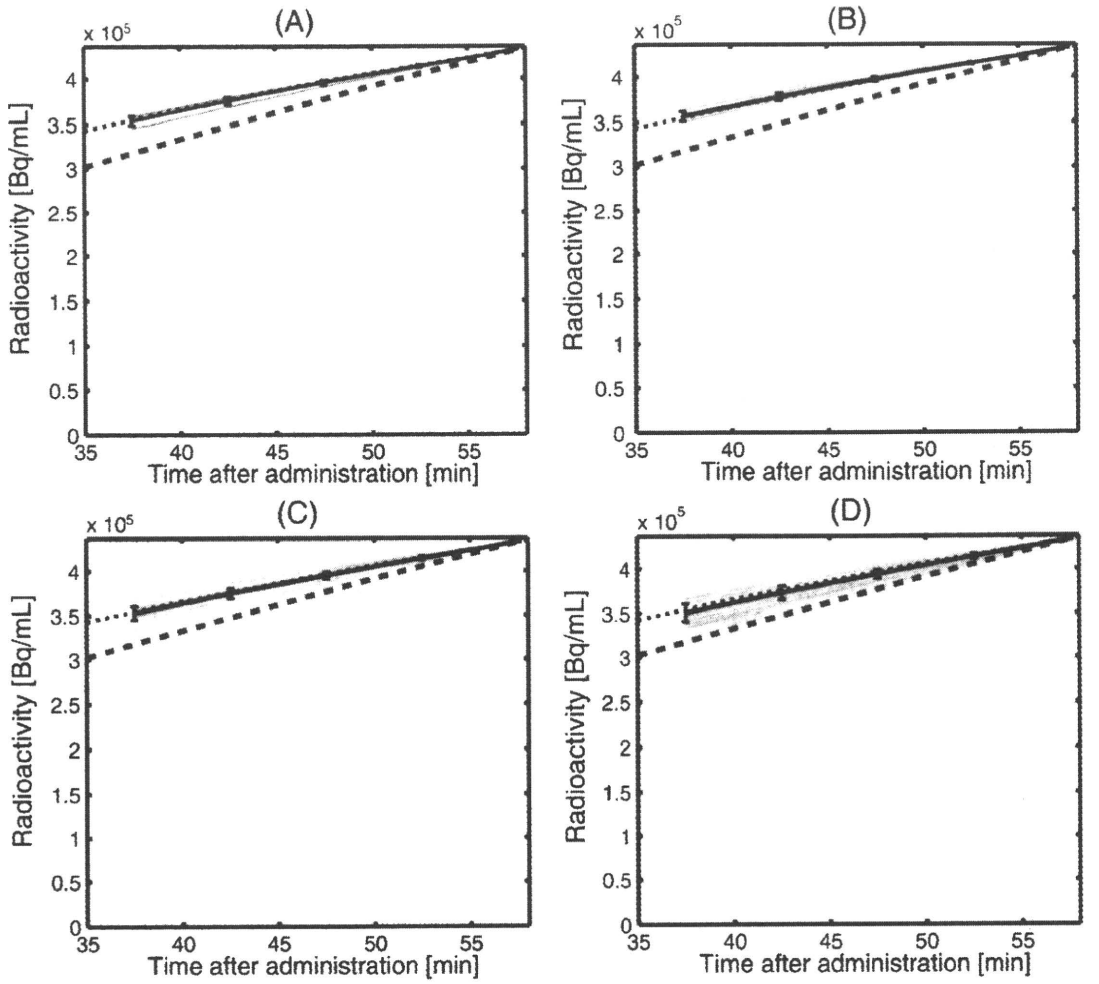

Fig. 8. Typical example of robust EPISA-estimated intpTACs (black solid line) in [^{11}C]PIB. The number of clusters was set to (A) 10, (B) 20, (C) 40, and (D) 80. Measured intpTACs with and without metabolite correction were plotted in black dotted line and gray break line. Standard deviation was calculated from the candidate intpTACs that were shown in gray solid lines.

will be applicable to radiopharmaceuticals whose metabolites cannot be ignored, or PET data with metabolism varied because of disease, dose, or other pathophysiological situations.

The next issue is the wide applicability of ISA. Using ISA, parametric images of BP_{ND} can be calculated using the estimated intpTAC and the specified reference region. When arterial blood sampling is not available, the basis function method (Gunn et al., 1997) is commonly used. While the basis function method is appropriate only when the PET data is described by a simplified reference tissue model (Lammertsma and Hume, 1996), ISA can be applied to any PET data with reversibly binding tracers. In this paper, to assure the wide applicability, EPISA was applied to two radioligands: [^{11}C]TMSX with slow peripheral metabolism and [^{11}C]PIB with fast one.

ISA has a disadvantage in practical application because of its high sensitivity to measurement noise. ISA is an algorithm to estimate the intersection between the planes spanned by tTAC and inttTAC. As shown in Fig. 3, ISA failed in estimating the intpTAC, even with low-noise. The reason for this is considered here. The ISA algorithm leads to the singular value decomposition problem. Generally, the singular vector with the smallest singular value is inaccurately estimated in the presence of noise. Therefore, it is important to reduce noise from the measured PET data before applying ISA.

In addition, the absolute value of the intpTAC cannot be estimated using ISA, as with other mathematical algorithms for the pTAC estimation (Barber, 1980; Paola et al., 1982; Wu et al., 1995; Lee et al., 2001; Naganawa et al., 2005a,b), because only the direction of a singular vector is presumable. Therefore, the relative V_T is obtained using Logan plot with the estimated pTAC or intpTAC. At least one-point arterial blood sampling is required to scale the estimated pTAC or intpTAC and calculate the absolute V_T. However, BP_{ND} can be calculated from the ratio of V_T values between target voxels and the reference region, and this calculation does not require the absolute value of the intpTAC. ISA can form the parametric image of BP_{ND} by specifying reference region.

In this study, a kinetic model-based clustering scheme was applied for noise reduction. It has been successfully applied in the rapid and robust parametric imaging of regional cerebral blood flow (Kimura et al., 1999) and [^{18}F]FDG studies (Kimura et al., 2002). In this paper, we proposed averaging and clustering as a way to successful ISA. The measured tTACs were clustered based on their kinetic shape. In the [^{11}C]TMSX studies, approximately 1250 voxels were assigned to a single cluster. Although the size of the cluster is too large as an anatomical ROI, such a large ROI is appropriate for EPISA because reducing noise is more important than increasing heterogeneity in the clusters. The estimated result was not influenced too much by the choice of the number of the clusters as shown in Fig. 8. IntpTACs were estimated from all possible pairs of the noise-reduced tTACs. In some pairs, estimated intpTACs were not monotonically increasing. The derivative of the intpTAC equals the pTAC. Therefore, the pTAC includes negative values when the intpTAC was not monotonically increasing.

The reference-region-based Logan plot also successfully estimates DVR or BP_{ND} without arterial blood sampling. Comparing EPISA with the reference-region-based Logan plot, robust EPISA does not need any kinetic parameters, while the reference-region-based Logan plot requires the population value of k_2 in the reference region in advance. We think that it is an advantage over the noninvasive Logan analysis. Note that noninvasive Logan analysis and our method will provide comparable results when the values of k_2 in a reference region are sufficiently similar in all subjects.

Exact values should be specified for the set of parameters used in the robust EPISA: the size of the averaging filter and the number of clusters. When the PET data have a low signal-to-noise ratio, a larger averaging filter and fewer clusters are preferable. We conclude that the ISA is a practical algorithm for the obviation of arterial blood sampling using noise reduction with clustering.

Acknowledgments

This work was supported in part by Grants-in-Aid for Scientific Research of the Japan Society for the Promotion of Science, No. 18591373 in 2006–2007, and No. 18-6916 in 2006–2008.

References

Barber, D.C., 1980. The use of principal components in the quantitative analysis of gamma camera dynamic studies. Phys. Med. Biol. 25 (2), 283–292.

Carson, R.E., 2002. Positron Emission Tomography Basic Science and Clinical Practice. Springer, Ch. 6, pp. 147–179.

Gunn, R.N., Lammertsma, A.A., Hume, S.P., Cunningham, V.J., 1997. Parametric imaging of ligand–receptor in PET using a simplified reference region model. NeuroImage 6 (4), 279–287.

Innis, R.B., Cunningham, V.J., Delforge, J., Fujita, M., Gjedde, A., Gunn, R.N., Holden, J., Houle, S., Huang, S.-C., Ichise, M., Iida, H., Ito, H., Kimura, Y., Koeppe, R.A., Knudsen, G.M., Knuuti, J., Lammertsma, A.A., Laruelle, M., Logan, J., Maguire, R.P., Mintun, M.A., Morris, E.D., Parsey, R., Price, J.C., Slifstein, M., Sossi, V., Suhara, T., Votaw, J.R., Wong, D.F., Carson, R.E., 2007. Consensus nomenclature for *in vivo* imaging of reversibly binding radioligands. J. Cereb. Blood Flow Metab. 27 (9), 1533–1539.

Ishiwata, K., Ogi, N., Shimada, J., Nonaka, H., Tanaka, A., Suzuki, F., Senda, M., 2000. Further characterization of a CNS adenosine A_{2a} receptor ligand [^{11}C]KF18446 with *in vitro* autoradiography and *in vivo* tissue uptake. Ann. Nucl. Med. 14 (2), 81–89.

Ishiwata, K., Wang, W.-F., Kimura, Y., Kawamura, K., Ishii, K., 2003. Preclinical studies on [^{11}C]TMSX for mapping adenosine A_{2A} receptors by positron emission tomography. Ann. Nucl. Med. 17 (3), 205–211.

Ishiwata, K., Mishina, M., Kimura, Y., Oda, K., Sasaki, T., Ishii, K., 2005. First visualization of adenosine A_{2A} receptors in the human brain by positron emission tomography with [^{11}C]TMSX. Synapse 55 (2), 133–136.

Kimura, Y., Hsu, H., Toyama, H., Senda, M., Alpert, N.M., 1999. Improved signal-to-noise ratio in parametric images by cluster analysis. NeuroImage 9 (5), 554–561.

Kimura, Y., Senda, M., Alpert, N.M., 2002. Fast formation of statistically reliable FDG parametric images based on clustering and principal components. Phys. Med. Biol. 47 (3), 455–468.

Kimura, Y., Naganawa, M., Yano, J., 2005a. Multidimensional clustering for molecular imaging using positron emission tomography and Logan plot to improve noise reduction capability. Proceedings of the International Federation for Medical and Biological Engineering, vol. 12, p. 2A2-01. Singapore.

Kimura, Y., Yano, J., Tsukahara, M., Naganawa, M., Ishii, K., Ishiwata, K., 2005b. Clustering approach for voxel-based Logan plot to improve noise reduction capability. VIIth International Conference on Quantification of Brain Function with PET. Amsterdam, Netherlands, p. S632.

Klunk, W.E., Engler, H., Nordberg, A., Wang, Y., Blomqvist, G., Holt, D.P., Bergström, M., Savitcheva, I., Huang, G.-F., Estrada, S., Ausén, B., Debnath, M.L., Barletta, J., Price, J.C., Sandell, J., Lopresti, B.J., Wall, A., Koivisto, P., Antoni, G., Mathis, C.A., Långström, B., 2004. Imaging brain amyloid in Alzheimer's disease with Pittsburgh Compound-B. Ann. Neurol. 55 (3), 306–319.

Koeppe, R.A., Holthoff, V.A., Frey, K.A., Kilbourn, M.R., Kuhl, D.E., 1991.

Compartmental analysis of [^{11}C]flumazenil kinetics for the estimation of ligand transport rate and receptor distribution using positron emission tomography. J. Cereb. Blood Flow Metab. 11 (5), 735–744.

Lammertsma, A.A., Hume, S.P., 1996. Simplified reference tissue model for PET receptor studies. NeuroImage 4, 153–158.

Lee, J.S., Lee, D.S., Ahn, J.Y., Cheon, G.J., Kim, S.K., Yeo, J.S., Seo, K., Park, K.S., Chung, J.K., Lee, M.C., 2001. Blind separation of cardiac components and extraction of input function from $H_2{}^{15}O$ dynamic myocardial PET using independent component analysis. J. Nucl. Med. 42 (6), 938–943.

Logan, J., Fowler, J.S., Volkow, N.D., Wolf, A.P., Dewey, A.L., Schlyer, D.J., MacGregor, R.R., Hitzeman, R., Bendriem, B., Gatley, S.J., Christman, D.R., 1990. Graphical analysis of reversible radioligand binding from time–activity measurements applied to [*n*-^{11}C-methyl]-(−)-cocaine PET studies in human subjects. J. Cereb. Blood Flow Metab. 10 (5), 740–747.

Logan, J., Fowler, J.S., Volkow, N.D., Wang, G.-J., Ding, Y.-S., Alexoff, D.L., 1996. Distribution volume ratios without blood sampling from graphical analysis of PET data. J. Cereb. Blood Flow Metab. 16 (5), 834–840.

Lopresti, B.J., Klunk, W.E., Mathis, C.A., Hoge, J.A., Ziolko, S.K., Lu, X., Meltzer, C.C., Schimmerl, K., Tsopelas, N.D., DeKosky, S.T., Price, J.C., 2005. Simplified quantification of Pittsburgh Compound B amyloid imaging PET studies: a comparative analysis. J. Nucl. Med. 46 (12), 1959–1972.

Mathis, C.A., Wang, Y., Holt, D.P., Huang, G.-F., Debnath, M.L., Klunk, W.E., 2003. Synthesis and evaluation of ^{11}C-labeled 6-substituted 2-arylbenzothiazoles as amyloid imaging agents. J. Med. Chem. 46 (13), 2740–2754.

Mishina, M., Ishiwata, K., Kimura, Y., Naganawa, M., Oda, K., Kobayashi, S., Katayama, Y., Ishii, K., 2007. Evaluation of distribution of adenosine A_{2A} receptors in normal human brain measured with [^{11}C]TMSX PET. Synapse 61 (9), 778–784.

Naganawa, M., Kimura, Y., Ishii, K., Oda, K., Ishiwata, K., Matani, A., 2005a. Extraction of a plasma time–activity curve from dynamic brain PET images based on independent component analysis. IEEE Trans. Biomed. Eng. 52 (2), 201–210.

Naganawa, M., Kimura, Y., Nariai, T., Ishii, K., Oda, K., Manabe, Y., Chihara, K., Ishiwata, K., 2005b. Omission of serial arterial blood sampling in neuroreceptor imaging with independent component analysis. NeuroImage 26 (3), 885–890.

Naganawa, M., Kimura, Y., Ishii, K., Oda, K., Ishiwata, K., 2007a. Temporal and spatial blood information estimation using Bayesian ICA in dynamic cerebral positron emission tomography. Digit. Signal Process. 17 (5), 979–993.

Naganawa, M., Kimura, Y., Mishina, M., Manabe, Y., Chihara, K., Oda, K., Ishii, K., Ishiwata, K., 2007b. Quantification of adenosine A_{2A} receptors in the human brain using [^{11}C]TMSX and positron emission tomography. Eur. J. Nucl. Med. Mol. Imaging 34 (5), 679–687.

Di Paola, R., Bazin, J.P., Aubry, F., Aurengo, A., Cavailloles, F., Herry, J.Y., Kahn, E., 1982. Handling of dynamic sequences in nuclear medicine. IEEE Trans. Nucl. Sci. NS-29 (4), 1310–1321.

Price, J.C., Klunk, W.E., Lopresti, B.J., Lu, X., Hoge, J.A., Ziolko, S.K., Holt, D.P., Meltzer, C.C., DeKosky, S.T., Mathis, C.A., 2005. Kinetic modeling of amyloid binding in humans using PET imaging and Pittsburgh Compound-B. J. Cereb. Blood Flow Metab. 25 (11), 1528–1547.

Wang, Z.J., Peng, Q., Liu, K.J.R., Szabo, Z., 2005. Model-based receptor quantization analysis for PET parametric imaging. 27th Annual International Conference of the IEEE Engineering in Medicine and Biology Society, pp. 5908–5911.

Watabe, H., Channing, M.A., Der, M.G., Adams, H.R., Jagoda, E., Herscovitch, P., Eckelman, W.C., Carson, R.E., 2000. Kinetic analysis of the 5-HT_{2A} ligand [^{11}C]MDL 100,907. J. Cereb. Blood Flow Metab. 20, 899–909.

Wu, H.M., Hoh, C.K., Choi, Y., Schelbert, H.R., Hawkins, R.A., Phelps, M.E., Huang, S.C., 1995. Factor analysis for extraction of blood time–activity curves in dynamic FDG-PET studies. J. Nucl. Med. 36 (9), 1714–1722.

doi:10.1111/j.1479-8301.2008.00246.x PSYCHOGERIATRICS 2008; 8: 105–107

EDITORIAL

Beyond PIB: the next generation of amyloid-imaging ligands

Hitoshi SHINOTOH and Tetsuya SUHARA

Department of Molecular Neuroimaging, Molecular Imaging Center, National Institute of Radiological Sciences, Chiba, Japan

Correspondence: Dr Tetsuya Suhara MD, PhD, Department of Molecular Neuroimaging, Molecular Imaging Center, National Institute of Radiological Science, 4-9-1 Anagawa, Inage-ku, Chiba 263-8555, Japan

Pittsburgh Compound B (PIB) is the commonly used name for *N*-methyl-[^{11}C]2-(4′-methylaminophenyl)-6-hydroxybenzothiazole (6-OH-BTA-1), an amyloid-imaging ligand that is widely used in the US, Europe, Australia, and Japan. Before Klunk and Mathis[1] developed [^{11}C]-PIB successfully at Pittsburgh University, a number of research groups had worked to find appropriate compounds as amyloid-imaging ligands *in vivo*. Attempts to find suitable compounds for positron emission tomography (PET) or single photon emission computed tomography (SPECT) studies started in the early 1990s. Radiolabelled monoclonal antibodies targeted to β-amyloid (Aβ) peptide were exploited as amyloid-imaging agents *in vivo*.[2] However, the primary limitation of this approach is that large molecular weight biomolecules cannot efficiently cross the blood–brain barrier (BBB) and bind to amyloid plaques contained within the parenchyma of the Alzheimer's disease (AD) brain. Mathis *et al.*[1] at Pittsburgh University initially focused their attention on Congo red, an amyloid-staining agent widely used in histological studies of post-mortem AD brain tissue sections. Congo red is a large molecule, a negatively charged sulfonate under physiological conditions, and is too hydrophilic to penetrate the BBB. Mathis *et al.*[1] then investigated the binding properties of Chrysamine G, a more lipophilic and potent Aβ ligand. However, efforts over more than 10 years to develop radiolabelled analogs of Congo red and Chrysamine G as amyloid-imaging agents for PET and SPECT were hampered by the relatively poor brain penetration of these compounds.

The first successful *in vivo* attempt to image Aβ in the brain of AD patients used PET and the malononitrile derivative [^{18}F]2-(1-{6-[(2-fluoroethyl)methyl-amino]-2-naphthyl}ethylidene)malononitrile ([^{18}F]-FDDNP), which was developed by Agdeppa *et al.*[3] at the University of California, Los Angeles.[4] This ligand is a derivative of 2-dialkylamino-6-acylmalononitrile-substituted napththalenes (DDNP), which is a hydrophobic, viscosity sensitive fluorescent probe. [^{18}F]-FDDNP has a high affinity for both Aβ and neurofibrillar tangles (NFT). Shoghi-Jadid *et al.*[4] reported the initial results from PET studies in 2002. The PET images showed high accumulation of radioactivity in the frontal, temporal, and parietal cortex in AD patients following injection of [^{18}F]-FDDNP. Unfortunately, signal-to-background ratios are low in the brain with this ligand and [^{18}F]-FDDNP PET only showed 9% higher cortical uptake in AD brain than in healthy controls.[5]

Mathis *et al.*[1] then turned their attention to thioflavin T, a dye for amyloid and with a small molecular weight. They removed positively charged heterocyclic nitrogen from thioflavin T to allow it to readily cross the BBB and 6-hydroxylated it for rapid clearance from the brain without Aβ. The resulting compound, [^{11}C]-6-OH BTA-1, was named 'PIB' at the University of Uppsala, where the first clinical study was performed with this ligand and PET. In 2004, Klunk *et al.* reported the initial results of a [^{11}C]-PIB PET study in 9 healthy volunteers and 16 patients with AD.[6] [^{11}C]-PIB PET showed a 70% increase in the cerebral cortex in AD patients compared with healthy controls. Many researchers in PET centers in the US, Europe,

Australia, and Japan followed their lead to start PET studies with [^{11}C]-PIB. At present, [^{11}C]-PIB PET studies are underway at seven PET centers in Japan and will soon be started at three others.

The [^{11}C]-PIB PET studies showed that almost all AD patients have high PIB binding in the cerebral cortex,[6] two-thirds of patients with mild cognitive impairment (MCI) have high PIB binding in the cerebral cortex similar to AD,[6] 80% of patients with Lewy bodies have high PIB binding in the cerebral cortex,[7] and 10–20% of healthy elderly people have high PIB binding in the cerebral cortex.[8] Patients with amyloid angiopathy also have high Aβ accumulation in the cerebral cortex, especially in the occipital cortex.[9] Longitudinal studies on healthy controls, MCI patients, and AD patients are underway in several institutions, and are expected to reveal the natural course of amyloid deposition in elderly people and AD.

The third successful *in vivo* attempt to image amyloid in the brain of AD patients, performed in Canada, used the stilbene derivative [^{11}C]-4-*N*-methylamino-4′-hydroxystilbene ([^{11}C]-SB-13).[10] In Japan, Kudo *et al.*[11] investigated benzoxazole derivatives as amyloid-imaging ligands and developed [^{11}C]-2-(2-[2-dimethylaminothiazol-5-yl]ethenyl)-6-(2-[fluoro]ethoxy)benzoxazole ([^{11}C]-BF-227) as a PET tracer. [^{11}C]-BF-227 may be unique because this ligand specifically binds to cored or mature plaques, whereas [^{11}C]-PIB seems to bind not only to neuritic plaques, but also to some extent to diffuse plaques.[12] However, these amyloid-imaging compounds have a lower signal-to-background ratio in the brain of AD patients than [^{11}C]-PIB. At present, [^{11}C]-PIB seems to be the best ligand for imaging Aβ in the AD brain by PET.

Does PIB fulfill all the requirements of an amyloid-imaging ligand in routine clinical studies? Carbon-11 is rapidly decayed, with a short half-life of only 20.4 min, which limits the use of PIB to PET centers with an on-site cyclotron and radiochemistry expertise. Fluorine-18 has a half-life of 110 min, meaning that fluorine-18-labelled compounds, such as [^{18}F]-fluoro-D-deoxyglucose ([^{18}F]-FDG) can be delivered to many PET centers from radiopharmaceutical companies. In the US, 95% of PET centers can receive a supply of an [^{18}F]-compound from radiopharmaceutical companies. In Japan as well, many PET centers are covered by the supply of [^{18}F]-FDG from a radiopharmaceutical company. Amyloid-imaging ligands labelled with fluorine-18 would greatly facilitate amyloid imaging with PET and it would be a profitable business.

SPECT is more widely available than PET, based on the fact that SPECT scanners are less expensive. Iodide-123 is a single photon emitter with a half-life of 13 h. ^{99m}Technetium is also a single photon emitter, has a half-life of 6 h, and could be produced at institutions by milking. Therefore, amyloid-imaging ligands labelled with [^{123}I] or [^{99m}Tc] would also greatly facilitate amyloid imaging.

Several companies are interested in the development of amyloid-imaging ligands labelled with [^{18}F], [^{123}I], or [^{99m}Tc]. In 2003, GE Healthcare licensed a number of compounds from the University of Pittsburgh, including PIB, and started large multisite trials with fluorine-18-labelled PIB in 2007. Avid Radiopharmaceutical Incorporation is a new venture company specializing in the development of imaging agents for AD and Parkinson's disease. They investigated stilbene derivatives and developed a series of ligands that share common structural features with PIB. Bayer Schering Pharma licensed one of the ligands developed by Avid Inc., known as [^{18}F]-BAY94-9172 or *trans*-4-(*N*-methyl-amino)-4′-{2-[2-(2-[^{18}F]-fluoro-ethoxy)-ethoxy]-ethoxy}-stilbene (also as [^{18}F]-AV1/ZK). [^{18}F]-BAY94-9172 has been used at the Center for PET, Austin Health, in Australia.[13] PET images similar to [^{11}C]-PIB PET images have been obtained in patients with AD and healthy controls with [^{18}F]-BAY94-9172 and PET. The mean neocortical uptake 90–120 min after injection of [^{18}F]-BAY94-9172 was 57% greater in AD patients than in healthy controls.[13]

[^{123}I]-IMPY was developed as an amyloid-imaging ligand for SPECT.[1] Unfortunately, the signal-to-background ratio in the brain of AD patients is low and there is considerable overlap in the target/cerebellum ratio between healthy controls and patients with AD. The development of better SPECT ligands for Aβ plaque is well underway.

Apart from amyloid imaging with PET or SPECT, Nakada *et al.*[14] recently reported the direct visualization of Aβ plaques in patients with AD *in vivo* by magnetic resonance microscopy on a 7T clinical system.

In parallel with the development of amyloid-imaging techniques, clinical trials of many anti-amyloid therapeutic drugs are underway.[15] A Phase III

study with monoclonal antibody therapy (bapineuzumab (AAB-001); Elan Corporation, Athlone, Ireland), is ongoing and this agent may be approved for clinical use within a few years in the US and Europe (see http://clinicaltrials.gov/ct2/results?term=bapineuzumab). Several clinical trials of gamma secretase inhibitors or modulators are also underway.

The development of amyloid-imaging techniques and anti-amyloid therapy may dramatically change the clinical treatment of AD within a few years. Elderly people, perhaps from 60 years on, may receive a brain checkup, including amyloid imaging, every 5 years. If they are found to have amyloid deposition in the cerebral cortex, they will then be treated with anti-amyloid drugs. The number of AD patients may decrease markedly if anti-amyloid therapy is proven effective. Although we still do not know whether the amyloid cascade hypothesis is true, we are waiting further developments with high expectations. A new diagnostic–therapeutic paradigm to successfully address AD and its harbinger, MCI–amnestic type, is emerging.

REFERENCES

1 Mathis CA, Wang Y, Klunk WE. Imaging β-amyloid plaques and neurofibrillary tangles in the aging human brain. *Curr Pharmaceut Design* 2004; **10**: 1469–1492.

2 Majocha RE, Reno JM, Friedland RP, VanHaight C, Lyle LR, Marotta CA. Development of a monoclonal antibody specific for beta/A4 amyloid in Alzheimer's disease brain for application to *in vivo* imaging of amyloid angiopathy. *J Nucl Med* 1992; **33**: 2184–2189.

3 Agdeppa ED, Kepe V, Liu J *et al.* Binding characteristics of radiofluorinate 6-dialkylamino-2-naphthylethylidene derivatives as positron emission tomography imaging probes for beta-amyloid plaques in Alzheimer's disease. *J Neurosci* 2001; **21**: RC189.

4 Shoghi-Jadid K, Small GW, Agdeppa ED *et al.* Localization of neurofibrillary tangles and beta-amyloid plaques in the brains of living patients with Alzheimer disease. *Am J Geriatr Psychiatry* 2002; **10**: 23–35.

5 Small GW, Kepe V, Ercoli LM *et al.* PET of brain amyloid and tau in mild cognitive impairment. *N Engl J Med* 2006; **355**: 2652–2563.

6 Klunk WE, Engler H, Nordberg A *et al.* Imaging brain amyloid in Alzheimer's disease with Pittsburgh Compound-B. *Ann Neurol* 2004; **55**: 303–305.

7 Rowe CC, Ng S, Ackermann U *et al.* Imaging beta-amyloid burden in aging and dementia. *Neurology* 2007; **68**: 1718–1725.

8 Mintun MA, Larossa GN, Sheline YI *et al.* [^{11}C]PIB in a nondemented population: Potential antecedent marker of Alzheimer disease. *Neurology* 2006; **67**: 446–452.

9 Johnson KA, Gregas M, Becker JA *et al.* Imaging of amyloid burden and distribution in cerebral amyloid angiopathy. *Ann Neurol* 2007; **62**: 229–234.

10 Verhoeff NP, Wilson AA, Takeshita S *et al. In-vivo* imaging of Alzheimer disease beta-amyloid with [^{11}C]SB-13 PET. *Am J Geriatr Psychiatry* 2004; **12**: 584–595.

11 Kudo Y, Okamura N, Furumoto S *et al.* 2-(2-[2-Dimethylaminothiazol-5-yl]ethenyl)-6-(2-[fluoro]ethoxy) benzoxazole: A novel PET agent for *in vivo* detection of dense amyloid plaques in Alzheimer's disease patients. *J Nucl Med* 2007; **48**: 553–561.

12 Lockhart A, Lamb JR, Osredkar T *et al.* PIB is a non-specific imaging marker of amyloid-beta (Aβ) peptide-related cerebral amyloidosis. *Brain* 2007; **130**: 2607–2615.

13 Rowe CC, Ackerman U, Browne W *et al.* Imaging of amyloid beta in Alzheimer's disease with ^{18}F-BAY94-9172, a novel PET tracer: Proof of mechanism. *Lancet Neurol* 2008; **7**: 129–35.

14 Nakada T, Matsuzawa H, Igarashi H, Fujii Y, Kwee IL. *In vivo* visualization of senile-plaque-like pathology in Alzheimer's disease patients by MR microscopy on a 7T system. *J Neuroimaging* 2008; **18**: 125–129.

15 Salloway S, Mintzer J, Weiner MF, Cummings JL. Disease-modifying therapies in Alzheimer's disease. *Alzheimer Dement* 2008; **4**: 65–79.

特集 Pre-MCIとpreclinical AD

高齢者におけるアミロイド蓄積の意義

Biological significance in amyloid beta protein amyloidosis involving the human aging brain

国立精神・神経医療研究センター病院
臨床検査科医長
Yuko Saito 齊藤祐子

東京都健康長寿医療センター
剖検病理科
Hiroyuki Hatsuta 初田裕幸

東京都健康長寿医療センター研究所
附属診療所所長
Kenji Ishii 石井賢二

東京都健康長寿医療センター
神経内科部長
Kazutomi Kanemaru 金丸和富

東京都健康長寿医療センター
高齢者ブレインバンク研究部長
Shigeo Murayama 村山繁雄

Summary

われわれの連続開頭剖検例の検討からは，アミロイドβ蛋白(Aβ)沈着は40歳代より新皮質にはじまり，65歳を超え急激に陽性頻度が上昇し，90歳代で頭打ちになる。陽性率は3分の2程度で，apoEε4の影響を強く受ける。原則としてAβ蓄積が新皮質に高蓄積しないと，神経原線維変化は新皮質には伸展しない。Aβ蓄積と認知機能は直接相関しない。Aβ活動免疫ワクチン投与後症例の検討からは，AD発病後Aβを除去しても，臨床経過には影響しない。US-ADNI1研究より，髄液Aβ低値がAβ沈着の最も早期のマーカーで，アミロイドPETがそれに次ぐことが提唱され，発症前ADの診断基準とされた。後継研究であるUS-ADNI2では，この発症前AD群を，AD発症予防対象とし，介入必要群の選別を研究目的に掲げている。US-ADNI研究では，もう1つのAβ沈着であるアミロイドアンギオパチーへの配慮は乏しい。また，Aβ沈着を前提としない，高齢者タウオパチー，レビー小体型認知症は含まれていない。後発のJ-ADNIにおいては，これらを含めた包括的アプローチが，独自の結果を出すには重要であろう。

Key words

●アルツハイマー病　●アミロイドアンギオパチー
●髄液バイオマーカー　●タウオパチー
●神経病理

Ⅰ アミロイド蓄積は，いつ頃からはじまるか？

アミロイドβ蛋白(Aβ)の加齢に伴う蓄積の検索法は，アミロイドPETの出現前には，バイアスのかからない連続剖検例による神経病理学的検討以外なかった。われわれはノースカロライナ大学連続剖検例で，改良メセナミン染色[1]で，0歳～90歳代までの例を年代別の群に分けて検討し，40歳代より蓄積症例が認められはじめ，65歳ぐらいより陽性率が急激に上昇することを明らかにした[2]。高齢者ブレインバンクはほとんどが65歳以上で平均年齢が80歳代である。改良メセナミン銀とAβ免疫染色が，実質アミロイド沈着において陽性率はほとんど変わらないことを確認後，同様の検討を加えたところ，Aβ沈着は90歳代でプラトーに達し，百寿例ではむしろ陽性頻度が下がることが明らかとなった。さらにアポリポ蛋白E(ApoE)遺伝子多型との対応を調べたところ，apoEε4のgene dose effectが明らかとなった。

Ⅱ アミロイド仮説

アミロイド仮説は神経原線維変化(neurofibrillary

tangle；NFT)の出現の前提に，アミロイドの沈着があるとするものである。Braakらは，高齢者連続剖検例の検討より，NFTの伸展ステージ分類を0～Ⅵまでの7段階，アミロイド沈着のステージを0～Cの4段階に分類した(図1)[3]。高齢者ブレインバンク連続剖検例の検討からは，新皮質へのNFTの伸展においては，老人斑のステージが影響を与えることが明らかである(表1)。ただ，辺縁系への出現には必ずしも老人斑の存在は前提にはならない[4]。老人斑，NFTの伸展ステージ分類に基づき，われわれは高齢者を4つの群に分類している(図2)。

Ⅲ アミロイドワクチン能動免疫例

AD例にAβ能動免疫を加えた治験は脳炎が起き中止になったが[5]，その後脳炎を起こさなかった例の剖検例が報告された[6]。それによると，老人斑は減少しているが，アミロイドアンギオパチーは減少せず，NFTについては突起に一部改善が認められるのみで，臨床経過には影響を与えていないことが明らかとなった。これは，以下のAD診断基準の改変に大きな影響を与えている。すなわち，ADが完成した後では，抗Aβ治療は無効であるという知見が示されたことになる。

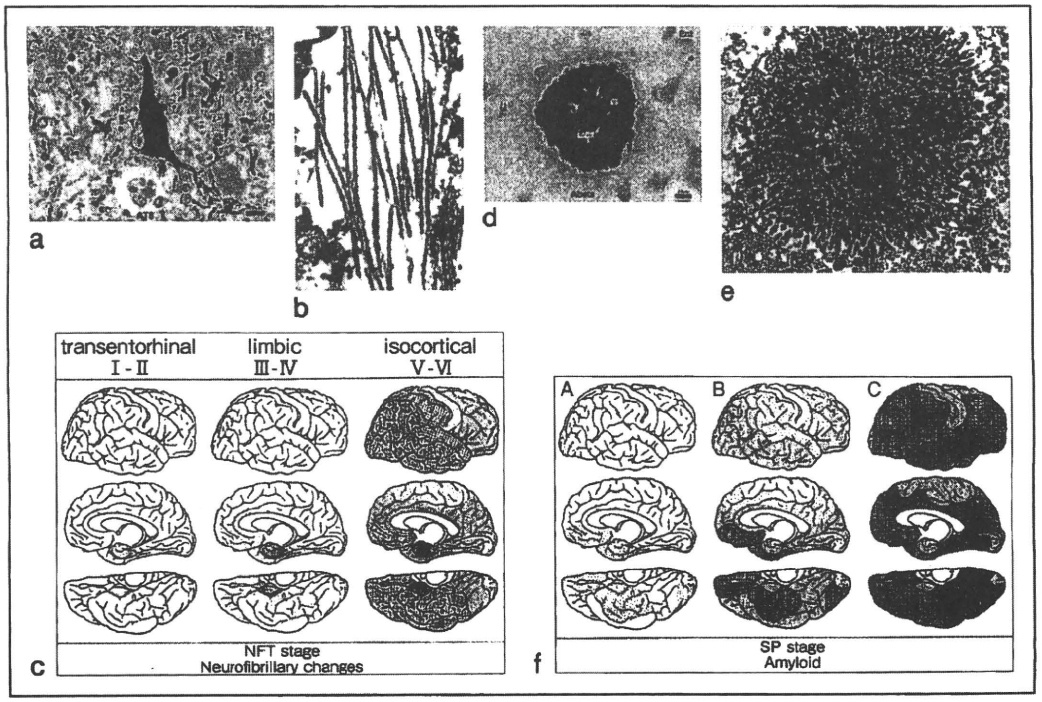

図1 Braakのアルツハイマー病理ステージ分類

神経原線維変化(NFT)とアミロイド沈着のステージ分類。a．抗リン酸化タウ抗体(AT8)免疫染色によるNFT。b．電子顕微鏡で観察したpaired helical filament。c．NFT伸展ステージ分類。移行嗅内野より嗅内野に伸展，辺縁系を進み，連合野，固有新皮質に到達する。Braakらは6,500例以上の高齢者連続剖検例よりこのステージ分類を提唱した。d．抗アミロイドβ蛋白抗体(11-28)免疫染色による古典的老人斑。e．老人斑の電顕像。アミロイド線維よりなる。f．Braakのアミロイド伸展ステージ分類。連合野より始まり，海馬に伸展し，固有域(運動領)に伸展する。これに対しCERAD分類は，チオフラビンS，あるいはBielshowsky鍍銀染色で，老人斑のコアあるいは変性突起を基準とし，新皮質の最も多い場所で高倍視野で11個あればCとするが，Braakのようなエビデンスに基づいていない。

(文献3)より改変，引用)

表1　高齢者ブレインバンク DNA リソース(1,890例)

Braak NFT/SP	0	I	II	III	IV	V	VI	計
0	34 66.3	314 75.8	102 81.8	46 85.6	12 85.4	1 81.0	0 –	509 77.5
A	16 75.5	350 78.0	149 83.6	74 86.2	23 88.6	1 99.0	0 –	613 80.6
B	8 76.1	169 79.9	91 82.8	70 85.6	23 91.2	2 82.0	1 94.0	364 82.4
C	3 76.0	50 79.4	51 83.0	80 84.5	80 86.6	100 86.4	40 83.9	404 84.4
計	61 70.5	883 77.7	393 82.9	270 85.4	138 87.6	104 86.4	41 84.1	1,890 80.9

Braakの神経原線維変化と老人斑のステージ分類を全例に施しており，これら連続性変化を研究対象にすることが可能である。この中で，アルツハイマー病と病理形態学的に診断しているのは，Braak神経原線維変化ステージⅣ以上，老人斑ステージCであり，全剖検例に占める割合は，11.6%(220/1,890)である。

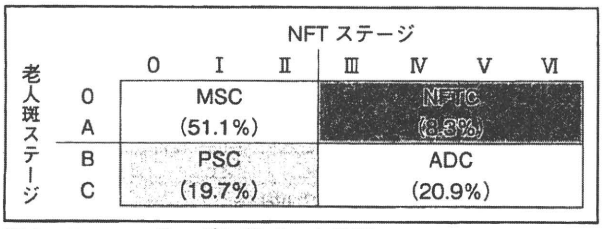

図2　Braak ステージに基づいた分類
Braakの分類により，高齢者をわれわれは4群に分けている。微小変化群(minimal senile change；MSC)は老年性変化がほとんどない群で，全体の51.1％を占めるが，平均年齢も最も若い。神経原線維変化優位群(NFT dominant change：NFTC)は年齢が最も高い。老人斑優位群(plaque-dominant senile change：PSC)は，Dickson博士らが病的老化群と呼んでいる群に相応するが，アミロイドβ蛋白バイオマーカーでは陽性になることが期待されKhachaturian分類ではアルツハイマー病(AD)に分類されうる。アルツハイマー病変化群(Alzheimer disease change：ADC)は，メルボルンブレインバンク(コリンマスターズ博士)ではADに分類される。AD新診断基準で，早期ADはADCに，発症前ADはPSCに相応することが予想される。

Ⅳ　アルツハイマー病新診断基準

われわれはこれまで，老人斑ステージC，NFTステージⅣ以上を，ADの病理診断基準としてきた[7]。一方，オーストラリアブレインバンクは，われわれのアルツハイマー病変化群(Alzheimer disease change；ADC)をADと診断している。ワシントン大学アルツハイマー病リサーチセンターでは，Khachaturian分類，すなわち老人斑が新皮質に一定の数あれば，ADと診断する基準を採用しており，われわれの老人斑優位老年性変化群(plaque-dominant senile change；PSC)とADCを含んだ群が，ADに分類される。

今回のNINCDS-ADRDA診断基準の改訂版となる新AD診断基準では，これまでのADはアルツハイマー認知症(Alzheimer disease dementia；ADD)となり，われわれの病理診断基準はそのまま移行し適応が可能である。一方これまで記銘力障害を示し，記憶障害型軽度認知障害(amnestic MCI；aMCI)といわれた群の中で，ADバイオマーカー(髄液Aβ低値，タウ，リン酸化タウ高値，アミロイドPET陽性)，放射線画像の異常(MRIによる側頭葉内側面萎縮，^{16}F-FDG PETによる後部帯状回代謝低下)を満たす群を，ごく初期(prodromal)ADと新たに定義されるが，これは神経病理学的にはADCにほぼ一致することが予想される。このごく初期ADが，AD進行予防治療の対象と規定されるのは，認知症を発症した後では抗Aβ治療は遅すぎるという見解に基づいている。一方発症前(subclinical) ADは，研究のための設定とされる。なんらかの自覚的他覚的記憶障害に，上記バイオマーカー，神経画像異常のいずれかの異常を呈するものを包括的に取り上げ，その中で真にADに進展する群を明らかにし，AD発症予防を行うべき対象を決定することが，US-Alzheimer's Disease Neuroimaging Initiative 1(US-ADNI1)の後継研究として，2010年11月よりスタートしたUS-ADNI2の主な目的の1つとされている。

Ⅴ　Aβ沈着のバイオマーカー

これまでも髄液Aβ値の低下はADのバイオマーカーとされていたが，US-ADNI1における^{11}C-PIB(Pittsburgh compound B)との比較検討で，^{11}C-PIBに先行して髄液Aβ低下がみられることが少数例での結果ではあるが，主張されるに至った。ただし，髄液Aβは日内変動を

示すこと，神経活動が低下すると値も低下することには留意が必要である。US-ADNI1では早朝安静空腹時採取と規定されている。われわれは，朝入院後，2時間安静をとった後，昼食前に髄液を採取している。それでもAβ髄液正常例には^{11}C-PIB蓄積はほとんど認められない結果を得ている(図3)。この結果は，かつて，進行性核上性麻痺を除外するため認知症の患者に必須であった髄液検査が，必須検査としての地位を回復したことを意味する。われわれの検討でも，Aβ低下剖検例はADとDLBであり，脳内Aβ沈着とほぼ相関している(表2)。

Ⅵ 老人斑とアミロイドアンギオパチー

アミロイドPETでは，老人斑・アミロイドアンギオパチーともに描出される。老人斑に関しては，Braakらの伸展分類[3]があるが，アミロイドアンギオパチーに関しては存在しない。われわれは連続剖検例の検討より，独自の伸展分類を採用している(図4)。今後アミロイドPETとの読影においては，老人斑とアミロイドアンギオパチーを総合的に評価していくことが，当然要求される。また，Aβワクチン研究で，アミロイドアンギオパチーの減少はみられないことが明らかとなり，アミロイドPETをAβ除去の指標に使う場合，注意すべき点と考えられる。

Ⅶ Aβ沈着を前提としない認知症

われわれの連続剖検例からは，高齢者タウオパチー(嗜銀顆粒性認知症，神経原線維変化優位型老年期認知症，進行性核上性麻痺，皮質基底核変性症)，レビー小体型認知症(dementia with Lewy bodies；DLB)純粋型，認知症を伴うパーキンソン病(Parkinson's disease with

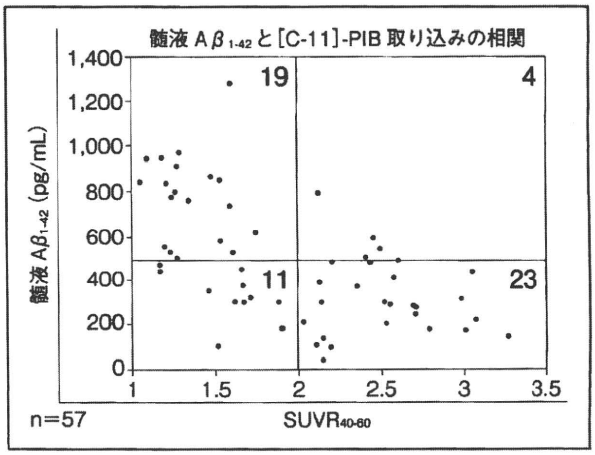

図3 髄液アミロイドβ蛋白(Aβ)値と^{11}C-PIBの陽性率の関係
髄液Aβ正常例で，PIB陽性例はきわめて少なく，診断上の有用性は明らかである。

表2 髄液アルツハイマー病バイオマーカーの剖検確認症例における値

	n	tau	p-tau	Aβ42
アルツハイマー病	**6**	**648.2 ± 397.1**	**62.4 ± 23.2**	**236.5 ± 115.3**
パーキンソン病	1	127.4	29.5	652.7
レビー小体型認知症	10	102.5 ± 60.0	39.8 ± 11.4	**407.1 ± 128.1**
進行性核上性麻痺	9	119.1 ± 107.3	39.3 ± 15.2	579.0 ± 147.6
皮質基底核変性症	3	156.3 ± 76.3	36.6 ± 4.0	483.1 ± 439.3
嗜銀顆粒性認知症	2	338.0 ± 357.4	50.8 ± 27.5	858.8 ± 197.8
運動ニューロン病	5	179.6 ± 167.7	36.0 ± 10.0	587.3 ± 244.1
脊髄小脳変性症	2	205.1 ± 39.1		817.6 ± 152.5
ピック病	1	122.6	38.8	630.5
クロイツフェルト・ヤコブ病	3	**1,990.4 ± 2,762.6**	54.8 ± 42.5	513.3 ± 484.2
コントロール	7	131.6 ± 71.3	31.3 ± 7.6	925.7 ± 226.3

われわれはタウ(tau)300pg/mL，リン酸化タウ(p-tau)55pg/mL，Aβ42(500pg/mL)をカットオフ値に設定している。低値をとるのはADとDLBであり，脳内アミロイド沈着と相関する。

dementia；PDD)は，Aβ沈着を前提としない。当然ながら，血管障害性認知症も，Aβ沈着は前提とならない。

US-ADNI1研究からのAD新診断基準は，Aβ沈着が認知症の前提というような主張に一見みえるが，Memory Clinicを中心とするADNI1同様の研究が，PD/PDD/DLBに関しては2011年にMovement Disorder Clinicを中心に行われる研究費申請が予定されている。高齢者タウオパチーに関しては，前頭側頭型認知症の枠組みで取り組むことが計画されている[8]。一方本邦においては，J-ADNI以外，日本全体で取り組める枠組みは今のところない。

日本は高齢化が急激に進行している点に鑑みると，高齢者タウオパチーの占める割合ははるかに大きいことが予想される。また，DLBの臨床診断に関しては，日本の臨床家が世界で最も知識豊富であることは間違いない。Aβ沈着の有無を，髄液Aβ低値，あるいはアミロイドPET陽性で確認し，陽性群と陰性群に分け，介入研究を行うことが，今後は必要となろう。

Ⅷ おわりに

高齢者におけるAβ沈着の意義は，2010年11月よりスタートしたUS-ADNI2で，バイオマーカー陽性群のどのグループがADに進展するかの研究により，明らかにされようとしている。最終診断が神経病理学的確認であるため，US-ADNI2では病理コアを設け，生前同意のブレインバンク登録と組み合わせることを行っている。これらの結果が最終的に得られるまでには一定の期間が必要と思われるが，US-ADNI2では確実な方法論を構築している。われわれもUS-ADNI2同様の神経病理コアをJ-ADNIに設け，同様の努力を行うことを開始した。読者の皆様のご協力をお願いしたい。

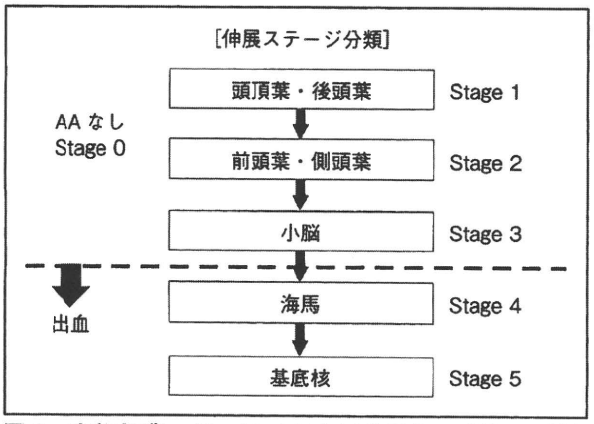

図4 高齢者ブレインバンクにおけるアミロイドアンギオパチー(AA)伸展ステージ分類
高齢者連続剖検例の検討より，新皮質から小脳に広がり，海馬に到達する伸展ステージ分類を提唱しており，脳葉出血(小出血も含め)をきたすレベルはステージ4以上であることを確認している。

文 献

1) Yamaguchi H, Haga C, Hirai S, et al：Distinctive, rapid, and easy labeling of diffuse plaques in the Alzheimer brains by a new methenamine silver stain. Acta Neuropathol **79**：569-572, 1990
2) Saito Y, Suzuki K, Nanba E, et al：Niemann-Pick type C disease；Accelerated neurofibrillary tangle formation and amyloid beta deposition associated with apolipoprotein E epsilon 4 homozygosity. Ann Neurol **52**：351-355, 2002
3) Braak H, Braak E：Neuropathological stageing of Alzheimer-related changes. Acta Neuropathol **82**：239-259, 1991
4) Katsuno T, Morishima-Kawashima M, Saito Y, et al：Independent accumulations of tau and amyloid beta-protein in the human entorhinal cortex. Neurology **64**：687-692, 2005
5) Furlan R, Brambilla E, Sanvito F, et al：Vaccination with amyloid-beta peptide induces autoimmune encephalomyelitis in C57/BL6 mice. Brain **126**(Pt 2)：285-291, 2003
6) Serrano-Pozo A, William CM, Ferrer I, et al：Beneficial effect of human anti-amyloid-beta active immunization on neurite morphology and tau pathology. Brain **133**(Pt 5)：1312-1327, 2010
7) Murayama S, Saito Y：Neuropathological diagnostic criteria for Alzheimer's disease. Neuropathology **24**：254-260, 2004
8) Cairns NJ, Bigio EH, Mackenzie IR, et al：Neuropathologic diagnostic and nosologic criteria for frontotemporal lobar degeneration；Consensus of the Consortium for Frontotemporal Lobar Degeneration. Acta Neuropathol **114**：5-22, 2007